Computers in Biology and Medicine 52 (2014) 130–143

Contents lists available at ScienceDirect

Computers in Biology and Medicine

journal homepage: www.elsevier.com/locate/cbm

A computational study of the respiratory airflow characteristics in normal and obstructed human airways

Bora Sul [a], Anders Wallqvist [a], Michael J. Morris [b], Jaques Reifman [a,*], Vineet Rakesh [a]

[a] Department of Defense Biotechnology High Performance Computing Software Applications Institute, Telemedicine and Advanced Technology Research Center, United States Army Medical Research and Materiel Command, Fort Detrick, MD, USA
[b] Department of Medicine, San Antonio Military Medical Center, Fort Sam Houston, TX, USA

ARTICLE INFO

Article history:
Received 23 April 2014
Accepted 13 June 2014

Keywords:
Obstructive lung diseases
Peripheral airways
Airflow pattern similarity measure
Wall shear stress
Computational fluid dynamics

ABSTRACT

Obstructive lung diseases in the lower airways are a leading health concern worldwide. To improve our understanding of the pathophysiology of lower airways, we studied airflow characteristics in the lung between the 8th and the 14th generations using a three-dimensional computational fluid dynamics model, where we compared normal and obstructed airways for a range of breathing conditions. We employed a novel technique based on computing the Pearson's correlation coefficient to quantitatively characterize the differences in airflow patterns between the normal and obstructed airways. We found that the airflow patterns demonstrated clear differences between normal and diseased conditions for high expiratory flow rates (>2300 ml/s), but not for inspiratory flow rates. Moreover, airflow patterns subjected to filtering demonstrated higher sensitivity than airway resistance for differentiating normal and diseased conditions. Further, we showed that wall shear stresses were not only dependent on breathing rates, but also on the distribution of the obstructed sites in the lung: for the same degree of obstruction and breathing rate, we observed as much as two-fold differences in shear stresses. In contrast to previous studies that suggest increased wall shear stress due to obstructions as a possible damage mechanism for small airways, our model demonstrated that for flow rates corresponding to heavy activities, the wall shear stress in both normal and obstructed airways was <0.3 Pa, which is within the physiological limit needed to promote respiratory defense mechanisms. In summary, our model enables the study of airflow characteristics that may be impractical to assess experimentally.

1. Introduction

Obstructive lung diseases are one of the most common and life-threatening conditions, causing high morbidity and mortality in industrialized countries [1]. Many lung diseases, such as asthma, bronchitis, and chronic obstructive pulmonary disease (COPD), are characterized by the obstruction of airflow in the lungs. According to the World Health Organization, COPD is the fourth leading cause of death worldwide and is estimated to become the third leading cause by 2030 [1]. The dominant cause of such obstructive lung diseases is exposure to lung irritants, resulting in the contraction of smooth muscle in airway walls and inflammation, which in turn lead to narrowing of the airway lumen [2].

The development of chronic disease conditions associated with airway obstruction may be altered by proper and timely intervention [3]. Thus, early detection and correct diagnosis are critical. However, some airway conditions remain hard to diagnose, especially those pertaining to the lower airways [4]. For example, significant discordance has been reported between commonly used references for the interpretation of spirometry data [5], and the American Thoracic Society does not recommend the use of spirometric parameters, such as the mid-expiratory flow, to detect lower airway disease [6]. According to the Third National Health and Nutrition Examination Survey (NHANES III), undiagnosed airflow obstruction (12%) is more common than diagnosed COPD (3.1%) or asthma (2.7%) in the United States (U.S.) and is associated with impaired health and functional status [4]. Undiagnosed pulmonary conditions have also been reported in U.S. military populations [7]. Out of 105 active duty military patients who complained of exertional dyspnea, one quarter (25 patients) had no specific diagnosis even after a comprehensive standard evaluation [7].

Understanding the airflow characteristics in the lower airways of the lungs could provide detailed insights on respiratory

* Correspondence to: Department of Defense Biotechnology High Performance Computing Software Applications Institute, Telemedicine and Advanced Technology Research Center, United States Army Medical Research and Materiel Command, ATTN: MCMR-TT, 504 Scott Street, Frederick, MD 21702, USA.
Tel.: +1 301 619 7915; fax: +1 301 619 1983.
E-mail address: jaques.reifman.civ@mail.mil (J. Reifman).

http://dx.doi.org/10.1016/j.compbiomed.2014.06.008
0010-4825/

Report Documentation Page

Form Approved
OMB No. 0704-0188

1. REPORT DATE	2. REPORT TYPE	3. DATES COVERED
2014		**00-00-2014 to 00-00-2014**

4. TITLE AND SUBTITLE
A computational study of the respiratory airflow characteristics Iin normal and obstructed human airways

5a. CONTRACT NUMBER
5b. GRANT NUMBER
5c. PROGRAM ELEMENT NUMBER

6. AUTHOR(S)

5d. PROJECT NUMBER
5e. TASK NUMBER
5f. WORK UNIT NUMBER

7. PERFORMING ORGANIZATION NAME(S) AND ADDRESS(ES)
U.S. Army Medical Research and Materiel Command,DOD Biotechnology High Performance Computing Software Applications Institute,Telemedicine and Advanced Technology Research Center,Fort Detrick, Frederick,MD,21702

8. PERFORMING ORGANIZATION REPORT NUMBER

9. SPONSORING/MONITORING AGENCY NAME(S) AND ADDRESS(ES)

10. SPONSOR/MONITOR'S ACRONYM(S)
11. SPONSOR/MONITOR'S REPORT NUMBER(S)

12. DISTRIBUTION/AVAILABILITY STATEMENT
Approved for public release; distribution unlimited

13. SUPPLEMENTARY NOTES

14. ABSTRACT

Obstructivelungdiseasesinthelowerairwaysarealeadinghealthconcernworldwide.Toimproveour understanding ofthepathophysiologyoflowerairways,westudiedairflow characteristicsinthelung between the8thandthe14thgenerationsusingathree-dimensionalcomputational fluid dynamics model, wherewecomparednormalandobstructedairwaysforarangeofbreathingconditions.We employedanoveltechniquebasedoncomputingthePearson'scorrelationcoefficient toquantitatively characterizethedifferencesinairflow patternsbetweenthenormalandobstructedairways.Wefound that theairflow patternsdemonstratedcleardifferencesbetweennormalanddiseasedconditionsfor high expiratory flowrates(42300ml/s),butnotforinspiratory flow rates.Moreover,airflowpatterns subjected to filtering demonstratedhighersensitivitythanairwayresistancefordifferentiatingnormal and diseasedconditions.Further,weshowedthatwallshearstresseswerenotonlydependenton breathing rates,butalsoonthedistributionoftheobstructedsitesinthelung:forthesamedegreeof obstruction andbreathingrate,weobservedasmuchastwo-folddifferencesinshearstresses. In contrasttopreviousstudiesthatsuggestincreasedwallshearstressduetoobstructionsasapossible damage mechanismforsmallairways,ourmodeldemonstratedthatfor flow ratescorrespondingto heavyactivities,thewallshearstressinbothnormalandobstructedairwayswas o0.3 Pa,whichis within thephysiologicallimitneededtopromoterespiratorydefensemechanisms.Insummary,our model enablesthestudyofairflow characteristicsthatmaybeimpracticaltoassessexperimentally.

15. SUBJECT TERMS

16. SECURITY CLASSIFICATION OF:			17. LIMITATION OF ABSTRACT	18. NUMBER OF PAGES	19a. NAME OF RESPONSIBLE PERSON
a. REPORT **unclassified**	b. ABSTRACT **unclassified**	c. THIS PAGE **unclassified**	**Same as Report (SAR)**	**14**	

Standard Form 298 (Rev. 8-98)
Prescribed by ANSI Std Z39-18

physiology and pathophysiology and be potentially useful for diagnosis of lower airway diseases. However, due to limitations in spatial and temporal resolutions, it is difficult to study local airflow characteristics in the lower airways using experimental techniques. For example, a pulmonary function test (PFT) involves measuring the volume of airflow during forced expiration at the mouth and comparing it with standardized normal values for diagnosis. However, because PFT measures airflow in the bulk phase, it is insensitive to regional differences in airflow patterns, especially in the lower airways. Similarly, although hyperpolarized noble gas magnetic resonance imaging can provide static and dynamic ventilation maps of the lungs [8], it is still not possible to obtain details of airflow characteristics, such as velocity contours, in the lower airways [9].

Computational fluid dynamics (CFD) provides the means to investigate, in detail and under controlled conditions, airflow characteristics in three-dimensional (3-D) models of the respiratory system. Previous CFD modeling efforts in pulmonary health have focused mainly on (1) establishing particle dosimetry in normal airways to optimize inhaled drug delivery and understand risks due to airborne pollutants [10,11], (2) understanding sleep apnea associated with obstructions in extrathoracic airways [12,13], and (3) investigating airway obstructions in the upper generations of the lungs [14,15]. In contrast, we focus on exploring airflow characteristics in the lower airways under different breathing conditions and examining influences of lower-airway obstructions as compared with normal conditions. Moreover, we aim to characterize airflow during both the inhalation and exhalation phases of respiration, as opposed to previous studies which have mostly investigated the inhalation phase [16,17]. Specifically, we developed CFD models of normal and obstructed airways between the 8th and the 14th generations with different obstruction patterns. We then compared the airflow patterns and flow-induced wall shear stresses for different flow conditions. Our results quantify differences in airflow characteristics due to obstructions commonly associated with lower airway lung diseases for both phases of respiration.

2. Methods

We developed two sets of airway models to validate our approach and study airflow characteristics. The first set of models (central and peripheral airways), which included airway generations from the trachea down to the 14th generation, was used to validate the computational approach of using a reduced number of airway generations to model airflow in the lungs. The second set of models (normal and obstructed airways) included only the airway branches between the 8th and 14th generations and was used to study the effects of obstructions in these lower airways on the airflow characteristics. To quantify the similarity and dissimilarity in airflow patterns in normal and obstructed airways, we used correlation coefficients and filtering techniques. We used different geometries and boundary conditions for these two sets of models, which are described in detail below.

2.1. Airflow models of central and peripheral airways

To assess the validity of using airway models with a reduced number of airway branches, we developed three 3-D airway models for central and peripheral airways with different numbers of airway branches. Fig. 1 shows the bronchi model (A), the central airway model (B), the central–peripheral airway model (C), and airway geometry and experimental data for *in vitro* velocity measurements by Isabey and Chang [18] (D). The bronchi model mimics the physical model from Isabey and Chang [18], which was

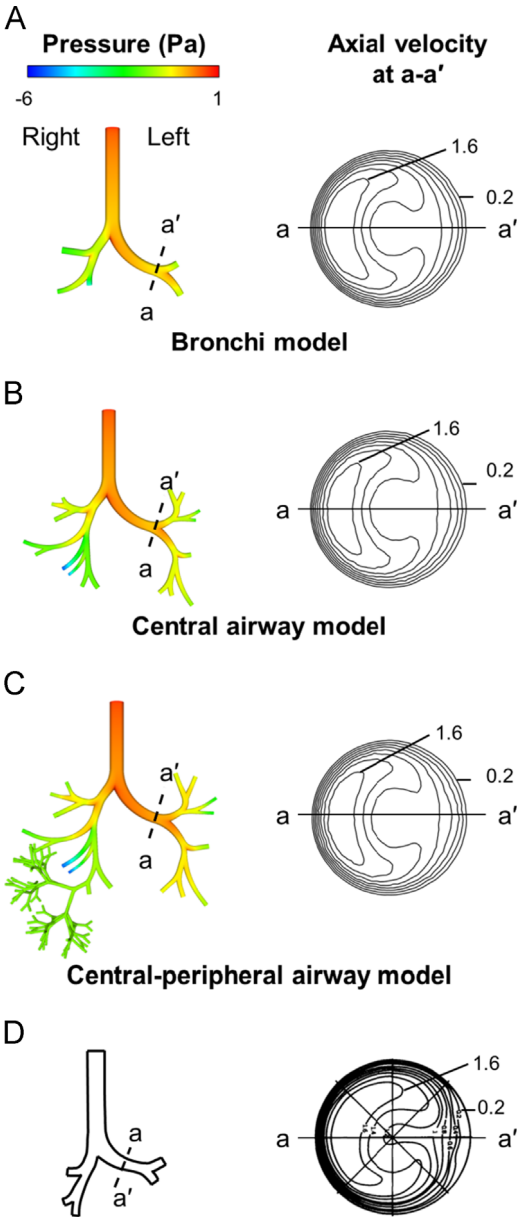

Fig. 1. Computational models of the bronchi (A), central (B), and central–peripheral airways (C) as well as experimental data (D) from Isabey and Chang [18]. Airway geometries for both computational and experimental models were based on the Horsfield model [19,20]. Left: pressure fields obtained from computational fluid dynamics (CFD) simulations (A)–(C) and airway geometry used in the experiment (D). Right: contours of axial velocity normalized by the maximum at the cross-section (a–a') obtained from CFD simulations (A)–(C) and the experiment (D). In the plots, each consecutive contour represents a velocity increment of 0.2. (For interpretation of the references to color in this figure legend, the reader is referred to the web version of this article.)

used to measure velocity profiles, and consists of branches from the trachea (i.e., the 1st generation) to five lobular bronchi. Isabey and Chang [18] used a truncated representation of the Horsfield model [19,20], which accurately describes healthy lung anatomy obtained from a lung cast of a male cadaver and captures the asymmetry of the lung structure. For the central airway model (Fig. 1(B)), we extended the bronchi model by including airway branches from the trachea to the 7th airway generation to replicate the complete central airway model available from Horsfield [19,20] (see Tables S1 and S2 and Fig. S1 in Supplementary material). The central–peripheral airway model represents both the central airways and one set of peripheral airways. The

peripheral airway component starts at one branch of the 7th generation in the central airway model and includes all airway branches between the 8th and 14th generations (Fig. 1(C)). Due to the unavailability of data regarding the branching angles in the lower airways, the peripheral airways were assumed to be symmetric [21,22]. Moreover, the effect of asymmetry on flow patterns was shown to be insignificant for low Reynolds number flow associated with the peripheral airways [23].

We created the 3-D airway geometries using computer-aided design software (AutoCAD 2012, The Autodesk). We used airway dimensions, such as diameter, length, branching angle, and branching radius (curvature), for each branch in the central airways [20] and average values of airway dimensions for each generation in the peripheral airways [19] (see Tables S1 and S2 and Fig. S1 in Supplementary material). Transitional zones near the bifurcations were built by lofting circular cross-sections of mother and daughter branches in AutoCAD. Due to the complexity of the geometries obtained after lofting, we did not incorporate the rounding of the carinal ridges [24].

In this set of simulations, our aim was to compare the airflow patterns predicted by our models with *in vitro* experimental data for steady-state inspiratory flow from Isabey and Chang [18]. To mimic the experimental conditions [18], we applied a velocity boundary condition at the inlet of the 1st generation (trachea) and outflow boundary conditions at the end of the terminal branches of the airway. A uniform velocity magnitude (1 m/s) normal to the boundary was specified at the inlet emulating the experiments. This corresponded to a flow rate of 200 ml/s, which is close to the

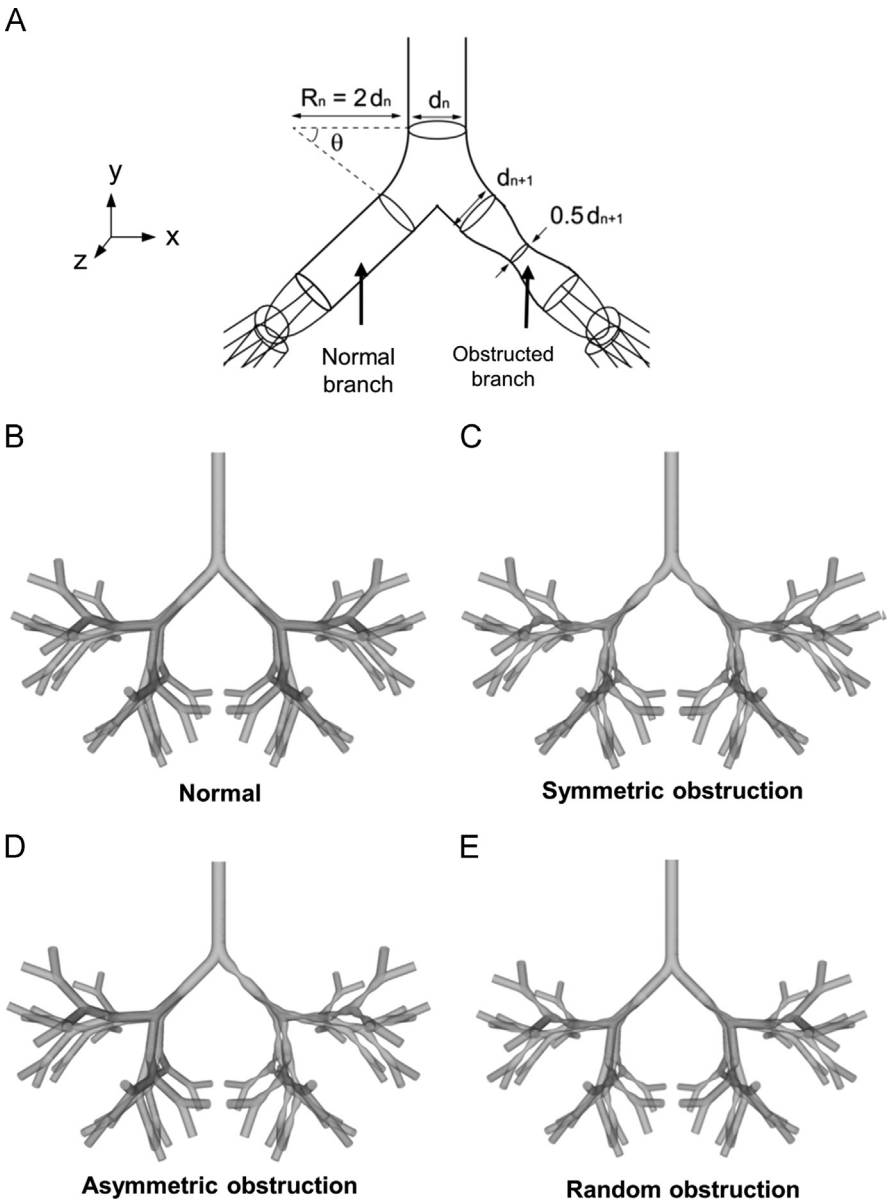

Fig. 2. Three-dimensional (3-D) geometries of peripheral airways (i.e., 8th generation to 14th generation). (A)–(E): detailed description of normal and obstructed branches at the *n*th airway generation (A) and 3-D geometries of normal airway (B), symmetric obstruction (C), asymmetric obstruction (D), and random obstruction (E) models. d_n, branch diameter; R_n, bifurcation diameter; θ, branching angle. The dimensions of all normal branches were taken from the Horsfield model [19]. Values for θ ($=45^\circ$) and R_n ($=2d_n$) were chosen within the physiological range [19]. The diameter of the obstructed branch was reduced by 50%. In the normal airway model, all branches were unobstructed. In the symmetric obstruction model, all branches were obstructed. In the asymmetric obstruction model, one of the second generation branches and all of its following daughter branches were obstructed. In the random obstruction model, obstruction sites were chosen randomly. In all models, airway branches in the first and last generations were unobstructed.

mean inspiratory flow rate in sedentary condition [25]. We did not add entrance lengths to the airway models because an extended entrance length was not included in the experiments. Flow was assumed to distribute unequally at the outlets to emulate the experiments and, therefore, flow rate weighting was specified as a constraint in the outflow boundary condition at each of the terminal branches. We estimated the flow rate weighting based on the volume fraction of the lung supplied by the terminal branch, as done in the experiment [18]. First, we determined the flow rate weighting in each of the five lobar bronchi using their corresponding lobar volume fractions from the literature [20]: 20% (upper right), 10% (middle right), 25% (lower right), 20% (upper left), and 25% (lower left). Next, we divided the flow in each lobar bronchus by $1/2^n$ to obtain flow rates at the outlets in the nth generation. We prescribed a no-slip boundary condition at the walls.

For numerical calculations, we created unstructured meshes using GAMBIT 2.4.6 (ANSYS Inc., Canonsburg, PA). We used 2 million, 4 million, and 13 million cells for the bronchi, central airway, and central–peripheral airway geometries, respectively, based on grid-independence tests (see Fig. S2 and Table S3 in Supplementary material). To obtain a numerical solution for the Navier–Stokes equations governing airflow, we used the steady-state, laminar flow solver in FLUENT 14 (ANSYS Inc., Canonsburg, PA). The assumption of laminar flow was valid, as the highest Reynolds number for the flow was 1055 at the 1st generation; it was lower for subsequent airway generations. For each simulation, we used 8 2.8-GHz Intel Xeon quad-core Nehalem processors at the Department of Defense (DoD) Supercomputing Resource Center located at the U.S. Army Research Laboratory.

2.2. Airflow models for normal and obstructed airways

We examined airflow patterns in healthy and diseased airways by developing corresponding 3-D models for normal (unobstructed) and obstructed airways. Because airway obstruction occurs mainly in the peripheral airways for most COPD cases [26], we created peripheral airway geometries from the 8th to 14th generation [20] without truncation of airway branches. To examine the effects of disease location and severity on airflow patterns, we constructed one normal and three different obstructed airway geometries, consisting of symmetric, asymmetric, and random obstructions. Fig. 2 shows the geometric configurations representing normal and obstructed branches (A), and the geometries of the normal airways (B), the symmetric obstruction (C), the asymmetric obstruction (D), and the random obstruction (E). In the normal airway geometry, none of the airway branches was obstructed. In the obstructed airway geometries, we constricted some of the branches between the 9th and 13th generations, which have been identified by a bronchoscopy study [27] as the most frequent disease sites. In the symmetric obstruction model, each of the 64 airway branches between the 9th and 13th generations was obstructed. In the asymmetric obstruction model, only the 9th generation airway branch on the left (i.e., in the $+x$ direction) and its daughter branches were obstructed, resulting in a total of 32 obstructions. In the random obstruction model, we randomly constricted 32 airway branches of the 64 branches between the 9th and 13th generation (Fig. 2(E)). Eighteen branches on the left (i.e., in the $+x$ direction) and 14 branches on the right (i.e., $-x$ direction) were obstructed (see Fig. S3 in Supplementary material). The resulting volume reduction in our geometries was 17% for the symmetric obstruction model and 8% for the asymmetric and random obstruction models (Table 1). This is consistent with airway surface area reductions in disease conditions reported by histological studies [26,28].

In this set of simulations, we used pressure boundary conditions at the inlet and outlets as opposed to the velocity and outflow boundary conditions used for the first set of simulations (i.e., for central and peripheral airways). By using the pressure boundary conditions, we could compute the change in air flow rate due to obstructions in the lower airways by subjecting the normal and obstructed airways to the same pressure differential. An implicit assumption was that both healthy and diseased lungs would experience the same pressure differential across the lungs for a given breathing effort. Within the physiological range [29], we applied pressure differentials (ΔP) of 18, 10, and 2 Pa to each airway geometry for both inspiratory and expiratory flows to simulate different breathing conditions. Table 1 shows the resulting flow rates at the inlet of peripheral airways and the estimated flow rates at the trachea, which correspond to a wide range of breathing conditions between sedentary ($\sim$300 ml/s) to forced breathing ($\sim$5000 ml/s) [30,31]. To estimate the flow rates at the trachea, we assumed that similar sets of peripheral airways follow each of the central airway outlets as has been used in previous airway models [32,33]. Accordingly, we estimated flow rates at the trachea to be 2^7 times the values at the peripheral airways. We extended the inlet of the peripheral airway to impose a fully developed flow. To this end, we added an entrance length of 300 mm ($\sim 61 \times$ diameter) to the first branch of the peripheral airway (i.e., the 8th generation from the trachea). The minimum entrance length required to obtain a fully developed flow based on the maximum Reynolds number was $\sim$166 mm. Because we used pressure boundary conditions, the flow velocities were not known *a priori* and, therefore, we included an extended entrance length to ensure fully developed flow for a range of applied pressure differentials. We also applied a no-slip boundary condition at the walls.

We created unstructured meshes with $\sim$7 million cells for each of the airway geometries, based on grid-independence tests (see Fig. S2 and Table S3 in Supplementary material). The flows in our models were laminar with a maximum Reynolds number of 563 at the 1st generation of the peripheral airway, corresponding to the peak inspiratory flow rate of 32.7 ml/s (Table 1) and maximum Reynolds numbers of 374, 201, and 241for the symmetric, asymmetric, and random obstruction models, respectively. The maximum Reynolds number for the obstructed airway models was observed at the constrictions at the uppermost generation (i.e., the 9th generation for the symmetric and asymmetric obstruction models and at the 10th generation for the random obstruction model). A steady-state solver was used with a second-order upwind scheme for the convective terms and the SIMPLEC algorithm for pressure-velocity coupling. Each simulation performed at the DoD's Supercomputing Resource Center took approximately 2–3 days.

2.3. Correlation coefficient as a similarity measure

We quantified differences between airflows in the obstructed and the normal airway models by computing Pearson's correlation coefficient for velocity contours at a particular cross-sectional plane. For numerical calculations, we obtained two matrices, **A** and **B**, where matrix elements represent the velocity magnitudes at each x-y spatial coordinate. We discretized the cross-sectional plane in the region of interest by creating fine meshes. At each grid point (x_i, y_j), we assigned the corresponding velocity magnitude (v_i, v_j) as a matrix element (i, j). The correlation coefficient (r) was defined [34] as follows:

$$r = \frac{\sum_i \sum_j (A_{ij} - \overline{A})(B_{ij} - \overline{B})}{\sqrt{\sum_i \sum_j (A_{ij} - \overline{A})^2 \sum_i \sum_j (B_{ij} - \overline{B})^2}}, \quad (1)$$

Table 1
Airway volume, flow rate, and resistance of the peripheral airways (i.e., 8th–14th generation).

	Normal	Symmetric Obstruction	Asymmetric Obstruction	Random Obstruction
Airway volume, ml (ratio to the normal geometry, %)				
	10.6 (100)	8.8 (83)	9.7 (92)	9.7 (92)
Flow rate, ml/s (flow rate at the trachea,* ml/s)				
Inspiratory flow, ΔP (Pa)				
18	32.7 (4,200)	18.6 (2,400)	29.5 (3,800)	27.3 (3,500)
10	19.6 (2,500)	11.8 (1,500)	17.7 (2,300)	16.5 (2,100)
2	4.3 (550)	3.0 (380)	4.0 (510)	3.8 (490)
Expiratory flow, ΔP (Pa)				
18	29.3 (3,800)	18.0 (2,300)	26.9 (3,400)	25.8 (3,300)
10	18.2 (2,300)	11.7 (1,500)	16.7 (2,100)	16.0 (2,000)
2	4.1 (520)	3.0 (380)	4.0 (510)	3.8 (490)
Airway resistance, $cmH_2O \cdot s/l$ (ratio to the normal, %)				
Inspiratory flow, ΔP (Pa)				
18	5.61 (100)	9.86 (176)	6.22 (111)	6.73 (120)
10	5.22 (100)	8.61 (165)	5.77 (111)	6.16 (118)
2	4.72 (100)	6.78 (144)	5.17 (110)	5.42 (115)
Expiratory flow, ΔP (Pa)				
18	6.26 (100)	10.17 (163)	6.83 (109)	7.13 (114)
10	5.59 (100)	8.75 (156)	6.09 (109)	6.38 (114)
2	4.93 (100)	6.78 (138)	5.17 (105)	5.42 (110)

ΔP, change in pressure. *Estimated by multiplying the flow rate of peripheral airways by 2^7.

where $\overline{A}$ and $\overline{B}$ denote mean velocity values of matrices **A** and **B**, respectively. We used ~30,000 grid points for each matrix based on grid-independence tests of correlation coefficient values.

3. Results

3.1. Inspiratory airflow in central and peripheral airways

Modeling the entire airway geometry is challenging both experimentally and computationally. The human respiratory system contains $>10^5$ conducting airway branches with ~20-fold size differences between the trachea and terminal bronchioles [20,32]. Thus, the human respiratory system is often studied using airway geometries with a reduced number of branches [33,35]. Even though Choi et al. [36] examined the effects of upper airway truncation on downstream airflow, it is not well established how modeling a reduced number of outlet branches affects the downstream airflows. To address this issue, we simulated airflows using the bronchi, central, and central–peripheral airway models and compared their flow patterns.

We examined the flow in the left main bronchus, which is not associated with the outlets in any of the models, to avoid immediate boundary effects. Fig. 1 shows pressure and velocity fields of the bronchi, central airway, and central–peripheral airway models. For comparisons with the experimental data from Isabey and Chang [18], we followed their method of normalizing the contour plots of axial velocity with respect to mean values. In all models, pressure drops across the same airway branches were not significantly different. Similarly, the velocity fields at the main bronchus did not differ considerably across models. In all models, the velocity magnitude approached zero near the wall, as expected from the no-slip boundary condition. Also, it was commonly shown in all three models that the high-velocity domain was skewed toward the lower left bronchus, which was similarly observed in a previous computational airflow study [24] for non-planar Horsfield model. All models especially displayed horseshoe-shaped velocity contours from 1.2 to 1.6 at the left bronchus, with minor differences in their width across the a–a' axis. This suggests that reduced branch geometries with appropriate boundary conditions are acceptable in modeling lung airways if the region of interest is not at the outlet branches.

We validated our models by comparing the velocity contours at the left main bronchus with experimental data. Fig. 1(D) shows the geometry used in an experiment by Isabey and Chang [18] to measure velocity profiles in an *in vitro* model and the experimental data of normalized axial velocity contours. The contours from the models and the experiment had similar patterns with minor discrepancies. As shown in Fig. 1(D), the high-velocity domain was slightly narrower across the a–a' axis compared with

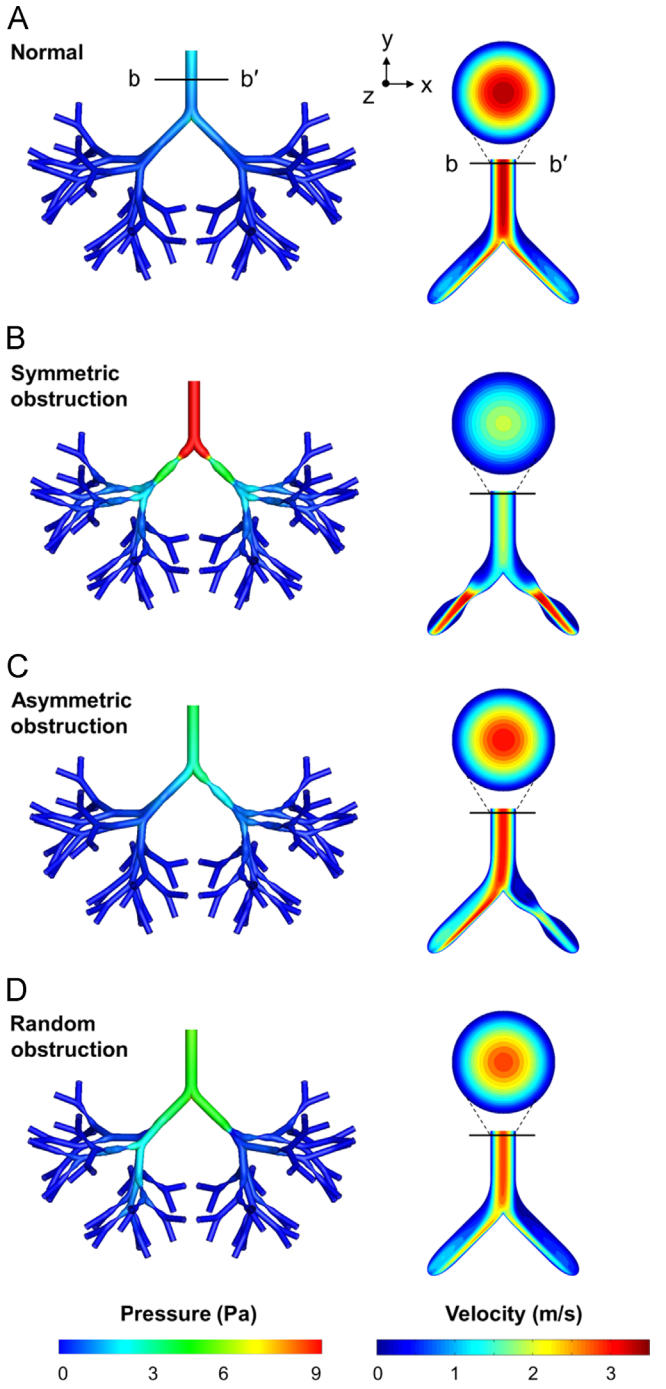

Fig. 3. High inspiratory steady flow in the normal airway (A), symmetric obstruction (B), asymmetric obstruction (C), and random obstruction (D) models. The applied pressure drop across the extended geometry was 18 Pa. Pressure fields and velocity fields of the coronal and uppermost axial planes are shown on the left and right, respectively. (For interpretation of the references to color in this figure legend, the reader is referred to the web version of this article.)

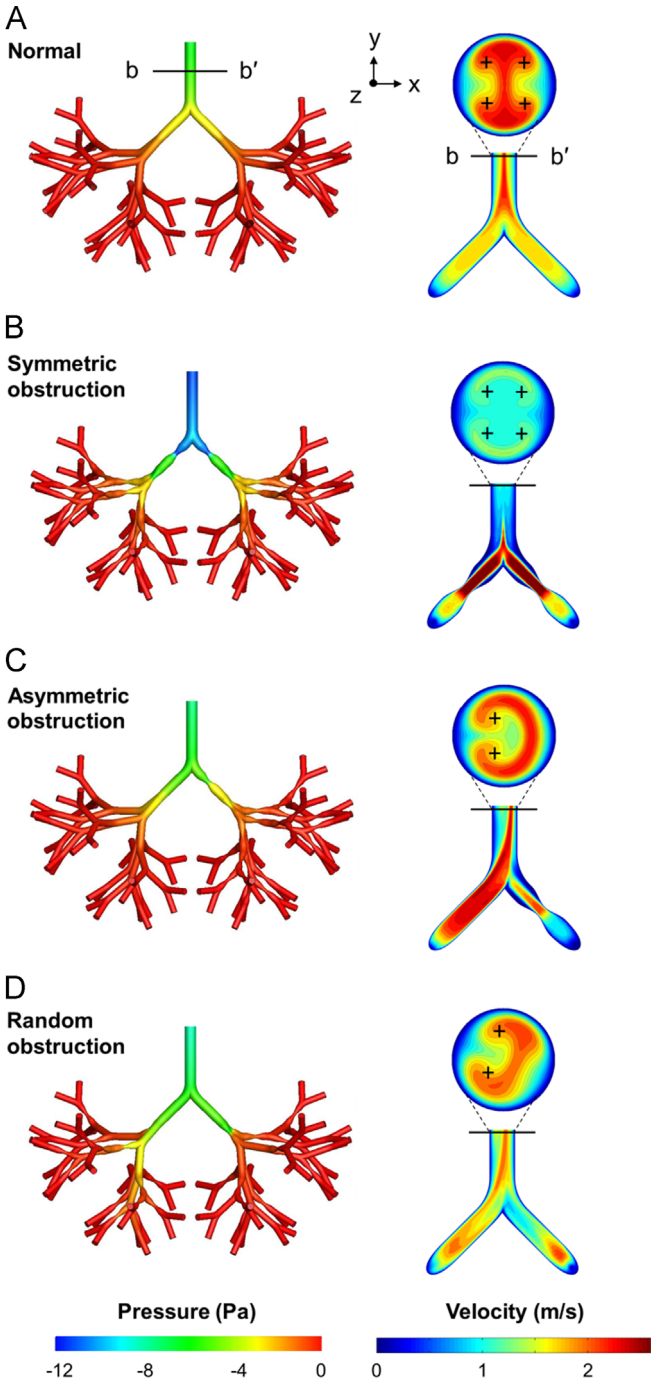

Fig. 4. High expiratory steady flow in the normal airway (A), symmetric obstruction (B), asymmetric (C), and random obstruction (D) models. The applied pressure drop across the extended geometry was 18 Pa. Pressure fields and velocity fields of the coronal and uppermost axial planes are shown on the left and right, respectively. Centers of vortices are marked by "+." (For interpretation of the references to color in this figure legend, the reader is referred to the web version of this article.)

those predicted by our models (Fig. 1(A)–(C)). We attributed these discrepancies to the attachment of the linear resistors in the experimental setup, an artificial effect not explicitly accounted for in the model. Moreover, the airflow patterns in the experimental data did not reflect the symmetry in the airway geometry about the a–a' axis [as assumed in the experimental model [18]], which suggested limited precision in the experimental data. Some of the differences between the model and experimental airflow patterns, therefore, may be attributed to experimental discrepancies. However, overall, we found that our models and the experiment exhibited a good qualitative agreement between flow patterns.

3.2. *Airflow in normal and obstructed airways*

Airway resistance is a measure of the opposition to the airflow caused by geometric properties, such as airway obstruction, and is

used to characterize and evaluate obstructive lung diseases. It is defined as the ratio of the total pressure drop to the flow rate [37]. To calculate peripheral airway resistance, we included only the peripheral airway geometry (i.e., the region below b–b' in Figs. 3 and 4) and extended the inlet of the first branch to obtain a fully developed flow. Table 1 shows the flow rate and resistance values of each airway model at different applied pressure drops. Resistance values were dependent on the degree and geometric distribution of the obstruction sites. In the symmetric obstruction model, resistance values were highest among all the models, as expected from the largest reduction in airway volume. The resistance values for the random and asymmetric obstruction models were close to each other as it should be expected from the similar amount of airway volume reduction (Table 1); nevertheless, the values for the random obstruction model were slightly higher (4–8%) than the asymmetric obstruction values depending on the pressure drop applied. It should be noted here that only the distribution of the obstructions was different in the asymmetric and random obstruction models: in the asymmetric obstruction model, all 32 branches on the left were obstructed, whereas for the random obstruction model, 18 branches on the left and 14 branches on the right were obstructed.

Resistance values increased with higher pressure drop for both inspiratory and expiratory flows, consistent with a previous model [38]. In addition, the difference in resistance values between the normal and obstructed airway models increased with higher flow rates. For the high inspiratory flow driven by an 18-Pa pressure drop, resistance values for the symmetric, asymmetric, and random obstruction models were 76%, 11%, and 20% higher than for the normal airway model, respectively (Table 1). For the low inspiratory flow driven by a 2-Pa pressure drop, resistance values of the symmetric, asymmetric, and random obstruction models were 44%, 10%, and 15% higher than the normal airway model, respectively (Table 1). Similarly, for expiratory flows, differences between the normal and obstructed airway models increased with flow rate (Table 1).

Increases in the resistance values for higher pressure drops, corresponding to a higher flow rate, were due to increases in the secondary flow. Based on the Hagen–Poiseuille equation, which assumes a fully-developed axial flow condition, the airway resistance should be constant for the same geometry. However, because the airway geometries in our models constitute a 3-D network of conduits that are curved near the bifurcations, secondary flows were expected to develop, as reported in the literature [39]. In such a system, flow resistance does not remain constant (as expected from the Hagen–Poiseuille equation) as the secondary flow increases with an increase in the pressure drop. Moreover, the effect of the secondary flow is more prominent near the constrictions in the obstructed airways due to the abrupt changes in the geometry. This explains the increase of differences in the airway resistance between the obstructed and normal airways with an increase in the pressure drop.

Fig. 3 shows pressure and velocity fields for high inspiratory flow driven by a total pressure drop of 18 Pa. Here, the airway models consist of the peripheral airways as well as the extended entrance lengths used to obtain a fully developed flow profile. As resistance in the peripheral airways increased due to obstruction compared with the normal airway model, we observed higher pressure gradients in the peripheral airways (Fig. 3). Consequently, the pressure drop in the extended entrance sections (not shown) of the airways decreased to compensate for the increase in pressure drop across the peripheral airways. The resulting pressure distribution across the peripheral airways was, therefore, different between the models even though the same total pressure boundary condition of 18 Pa was applied to all models.

We then focused on airflow patterns to gauge how obstructions, modeled as geometric changes in the lower-generation branches, manifested themselves as altered flow in an 8th to 14th generation airway model. Specifically, we compared velocity contours at a coronal (i.e., perpendicular to the z-axis) and an axial (i.e., perpendicular to the y-axis) plane in the uppermost branches of the peripheral airways. The velocity fields at the coronal plane show the airflow patterns from the first branch (i.e., the 8th generation) to the second branch (i.e., the 9th generation) in the peripheral airways. In the normal airway model, our velocity profile was skewed toward the inner side walls in the second branch (Fig. 3(A)), which has also been observed experimentally in previous studies [40,41]. In the symmetric obstruction model, the flow upstream of the constricted zone was slowed down due to high downstream resistance (Fig. 3(B)). However, while passing the neck of the constricted zone, the flow evolved into a jet-like pattern with highly increased velocities, which is consistent with previous studies [14,21]. In the asymmetric obstruction model, the airflow was disproportionate with ~80% of air flowing into the unobstructed branch (Fig. 3(C)). In the random obstruction model, flows in the second branches (i.e., the 9th generation) in the peripheral airways were unequal even though their airway structures were the same (Fig. 3(D)). The flow rate in one branch was 50% higher than the other. This was attributed to the uneven distribution of obstructions in the branches downstream of the second branch (i.e., the 9th generation) (Fig. 2(E)). With the same volume reduction, the asymmetric and random obstruction models had different asymmetric airflow patterns. This suggests that the flow pattern is not only dependent on the degree of obstruction but also highly dependent on their distribution.

We compared velocity patterns at axial planes (i.e., along the b–b') in the normal and obstructed airways. Velocities were highest (i.e., colored red) for the normal airway model and lowest (i.e., colored blue) for the symmetric obstruction model. The results shown in Fig. 3 demonstrate that, although the velocity magnitudes were different, the velocity patterns for steady-state inspiratory flow at the axial planes were not very different between the models. The shapes of the velocity contours in all the models were similar, coaxial circles, with the highest velocity at the center and zero velocity at the walls. This was consistently observed in all the inspiratory flows driven by different pressure drops (data not shown).

Fig. 4 shows pressure and velocity fields for high expiratory flow, driven by a total pressure drop of 18 Pa. Similar to the high inspiratory flow (Fig. 3), a higher absolute pressure drop was observed for the obstructed airway models than the normal airway model, reflecting higher resistance in the obstructed airways. The velocity contours in the coronal plane illustrated differences in the upstream flow in the normal and obstructed airway models. In the normal airway model, the flow merged symmetrically and gradually from the lower branches after passing the branching point. This resulted in a peak velocity (colored red) of the flow being increasingly concentrated around the centerline as the flow progressed toward the trachea. This has been consistently observed in experimental studies [40,42]. The increased velocity in the upper branch was due to a decreased total cross-sectional surface area [20,32]. The flow in the obstructed airway models was not as smooth and gradual as in the normal airway model. Similar to the inspiratory flow, jets were formed in the neck of the constricted zones, as consistently predicted in other computational studies [14,43]. Recirculating flows were present in the vicinity of the jet due to boundary layer separation (Fig. 4). Vorticity is a measure of the rotation of the fluid and is given by the curl of the velocity field. The vorticity in the constricted branches of the symmetric obstruction model was ~100-fold higher than the value at the same location in the normal airway model. We attributed the increase in vorticity in the symmetric obstruction model to the significant increase in the velocity magnitude near the constriction, as discussed above

(Fig. 4) as well as to the increase in secondary flow velocity components due to the abrupt change in the shape of the conduit near the constriction. In the symmetric obstruction model, the velocity dropped immediately after the two jets merged at the branching point. In the asymmetric model, the flow was dominantly from the unobstructed branch, similar to the inspiratory flow (Fig. 3(C)). The flow rate in the unobstructed branch was 80% higher than in the obstructed branch. For the random obstruction model, the flow rate in the right branch (with 14 downstream obstructions) was 50% higher than the left branch (with 18 downstream obstructions). The random obstruction model also showed the recirculation zones in the second branch (i.e., 9th generation) of the peripheral airways.

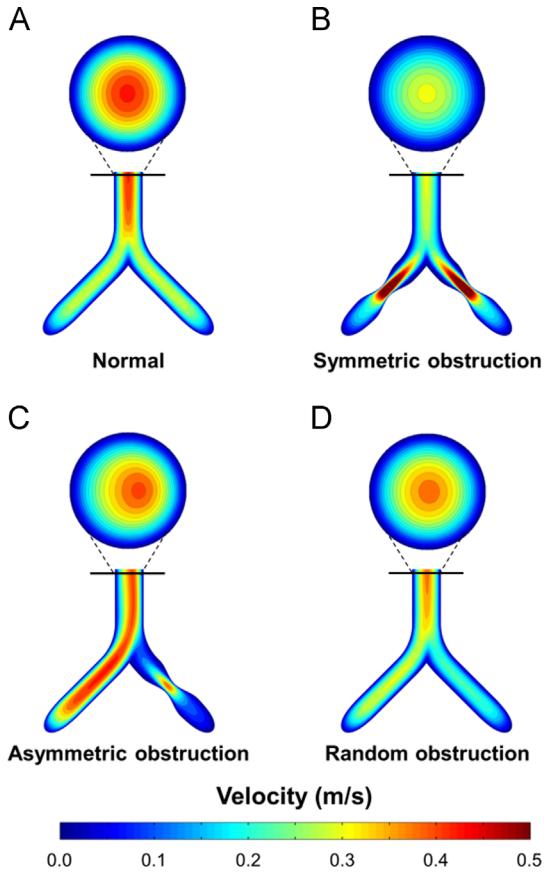

Fig. 5. Velocity fields of low expiratory steady flow in the normal airway (A), symmetric obstruction (B), asymmetric obstruction (C), and random obstruction (D) models. The applied pressure drop across the extended geometry was 2 Pa. (For interpretation of the references to color in this figure legend, the reader is referred to the web version of this article.)

In contrast to the inhalation flow, we observed widely different axial velocity patterns between the normal and the obstructed airway models for expiratory flow. As shown in Fig. 4(A) the high-velocity contours (i.e., colored red) were dumbbell shaped across the *y*-axis. Four vortices (marked by "+") were formed symmetrically, as has been found experimentally [40]. The flow in the symmetric obstruction model also had four vortices in the axial plane of the uppermost branches but with much lower velocity. High-velocity flow was more concentrated along the dorsal and ventral walls (Fig. 4(B)). In the asymmetric obstruction model, the high-velocity domain was highly skewed toward the obstructed branch (Fig. 4(C)). This was because of the unbalanced high-velocity jet from the unobstructed branch. In the random obstruction model, the velocity contours were asymmetric in both coronal and axial planes, reflecting the uneven distribution of obstruction sites in the geometry (Fig. 4(D)). The high-velocity region was skewed toward one side of the wall with the formation of two large vortices. Also, we found that axial airflow patterns were similarly distinguishable between normal and obstructed airways in other planes as well (data not shown).

We examined the dependence of flow intensity on airway patterns. Fig. 5 shows velocity contours of low expiratory flow driven by a 2-Pa total pressure drop. Similar to the high expiratory flow (Fig. 4), jet flows and recirculation zones were present at the obstructed branches but with smaller degrees. However, the velocity contours in the axial plane were not distinguishable between the models except for their magnitudes. Peak velocity was observed at the center of the axial plane with little deviation in the different models. Vortices were not found in the axial plane due to reduced secondary flow momentum.

Table 2
Similarity measures based on Pearson's correlation coefficient against normal velocity contour plots at the axial plane in the uppermost branches for expiratory flow.

	Symmetric Obstruction	Asymmetric Obstruction	Random Obstruction
No filter (r)			
18	0.94	0.90	0.83
10	0.98	0.84	0.95
2	0.99	1.00	1.00
Low-velocity filter (r_1)			
18	0.47	0.41	0.27
10	0.87	0.21	0.59
2	0.95	0.81	0.97
Near-wall domain filter (r_2)			
18	0.77	0.65	0.55
10	0.95	0.50	0.84
2	1.00	0.96	1.00

3.3. Quantitative characterization of airflow patterns

We observed marked differences and distinct characteristics in flow patterns between the models. Velocity contour plots (Figs. 3–5) represent not only the spatial distribution of velocity magnitudes but also illustrate the airflow patterns, which are given by the distribution and shape of the velocity contours, e.g., the velocity pattern for expiration in the normal airway in Fig. 4 was dumbbell shaped. Although similarities and differences in airflow patterns can be directly visualized from such plots, a more quantitative characterization of flow patterns would provide for a more accurate and systematic comparative analysis.

To quantitatively compare flow characteristics between the obstructed airway flow patterns and the normal airway patterns, we calculated their Pearson's correlation coefficient. The correlation coefficient measures the linear dependence between two variables, attaining values between -1 and 1, with -1 indicating perfect anticorrelation, 0 indicating no correlation, and 1 indicating perfect correlation [34]. If two sets of velocity contours have similar patterns except for their magnitudes, the correlation coefficient would be close to 1. If two flow patterns share no similarity, they would be uncorrelated and the correlation coefficient would be close to zero.

Table 2 shows correlation coefficients of the velocity contour plots at the axial plane in the uppermost branches for expiratory flows. We obtained these values by comparing the velocity contours from the obstructed airways with those from the normal airways. For all flow rates, the correlation coefficient, r, was close to 1 in all the obstructed airway models even though the velocity contours exhibited significant visual differences in flow patterns between the models (Fig. 4). This was mainly a consequence of the no-slip boundary condition imposed on the walls, which, in effect, generated a dominating low-velocity field near the walls for the normal as well as the obstructed airway models (Figs. 3–5).

To avoid the dominating effect of this near-wall velocity field, we filtered the low-velocity contours and recalculated correlation coefficients between airway models. Fig. 6 shows the velocity contours for high expiratory flow ($\Delta P = 18$ Pa) after the use of two different filters: a low-velocity filter (A) and a near-wall filter (B). The low-velocity filter eliminated velocity contours with velocity values $< 50\%$ of the maximum velocity to limit the focus to the high-velocity region. Because the low-velocity filter produced different areas in the normal and obstructed geometries (Fig. 6 (A)), we used only the intersecting areas to calculate the correlation coefficient. The near-wall filter excluded the velocity values in the region close to the airway wall. Because the boundary layer thickness [44] of the flow in our study was $\sim 14\%$ of the airway radius, we used 15% of the airway radius as the distance threshold for the near-wall filter.

Correlation coefficient values obtained after applying the low-velocity filter (r_1) and the near-wall filter (r_2) were dependent on the flow conditions as well as the airway models (Table 2). For the symmetric obstruction model, correlation coefficients were higher than those for the other obstructed models for all flow conditions (Table 2). This was attributed to the symmetry of airway geometries in both the normal and symmetric obstruction models, which led to similar airflow patterns. For high expiratory flow ($\Delta P = 18$ Pa), both r_1 and r_2 were < 0.8 in all obstructed airway models (Table 2). We observed minimum r_1 and r_2 values for the random obstruction model, while the symmetric obstruction model resulted in the maximum values (Table 2). For the asymmetric and random obstruction models, both r_1 and r_2 were ≤ 0.65, demonstrating highly dissimilar flow patterns compared with the normal airway. Importantly, the airway resistance values of these two obstruction models were merely 20% higher than the normal airway model (Table 1), which is within the normal variability range of airway resistance values [45]. This implies that, for high expiratory flow and after applying appropriate filters to avoid inclusion of low and near-wall velocities, airflow patterns are a much more sensitive indicator of airway conditions compared with resistance values in the peripheral airways.

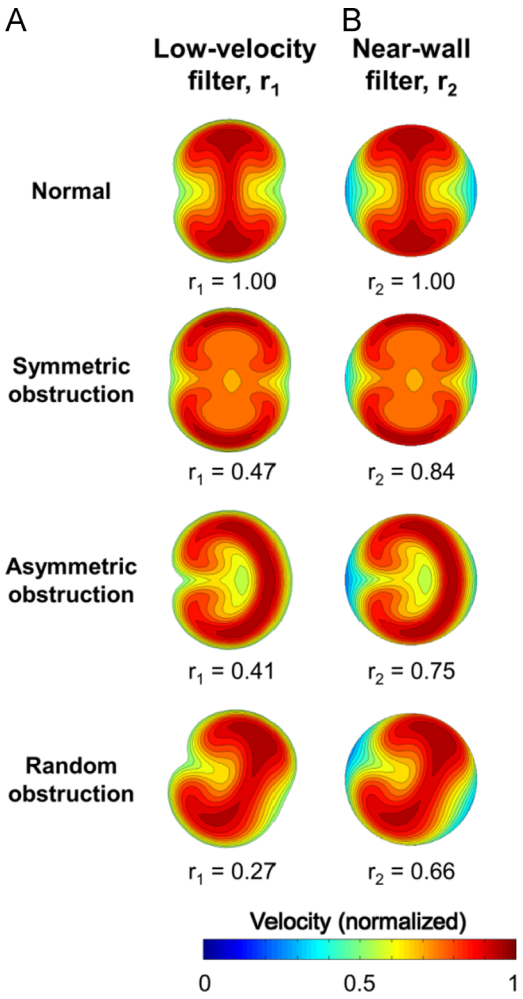

Fig. 6. Velocity contours in the region of interest (ROI) for the calculation of correlation coefficients after low-velocity (A) and near-wall (B) filtering. Velocity contours in the uppermost axial planes for high expiratory flow ($\Delta P = 18$ Pa) were normalized by the maximum. The ROI was redefined as velocity fields larger than 50% of the maximum for low-velocity filtering and as 15% away from the wall for near-wall filtering. Correlation coefficients after low-velocity filtering (r_1) and near-wall filtering (r_2) were obtained between the velocity fields from the normal airway model and each obstruction model. (For interpretation of the references to color in this figure legend, the reader is referred to the web version of this article.)

Conversely, for low expiratory flow ($\Delta P = 2$ Pa), correlation coefficient values of r_1 and r_2 were close to 1, indicating that the flow patterns were similar to the normal airway. These results were consistent even if different thresholds were applied for the two filters (data not shown). This suggests that flow patterns with low flow rates would be indistinguishable between the normal and obstructed airway condition, which was also visually observed (Fig. 5).

For inspiratory flow, the correlation coefficients at the uppermost axial plane remained 1 for all flow rates even after we used the filters. We compared flow patterns in other axial planes of the uppermost branches and tested different thresholds for both filters, but obtained the same results. This corroborates our visual observation that the airflow patterns at the axial plane of the uppermost branch for inspiratory flow are similar across the normal and obstructed airways.

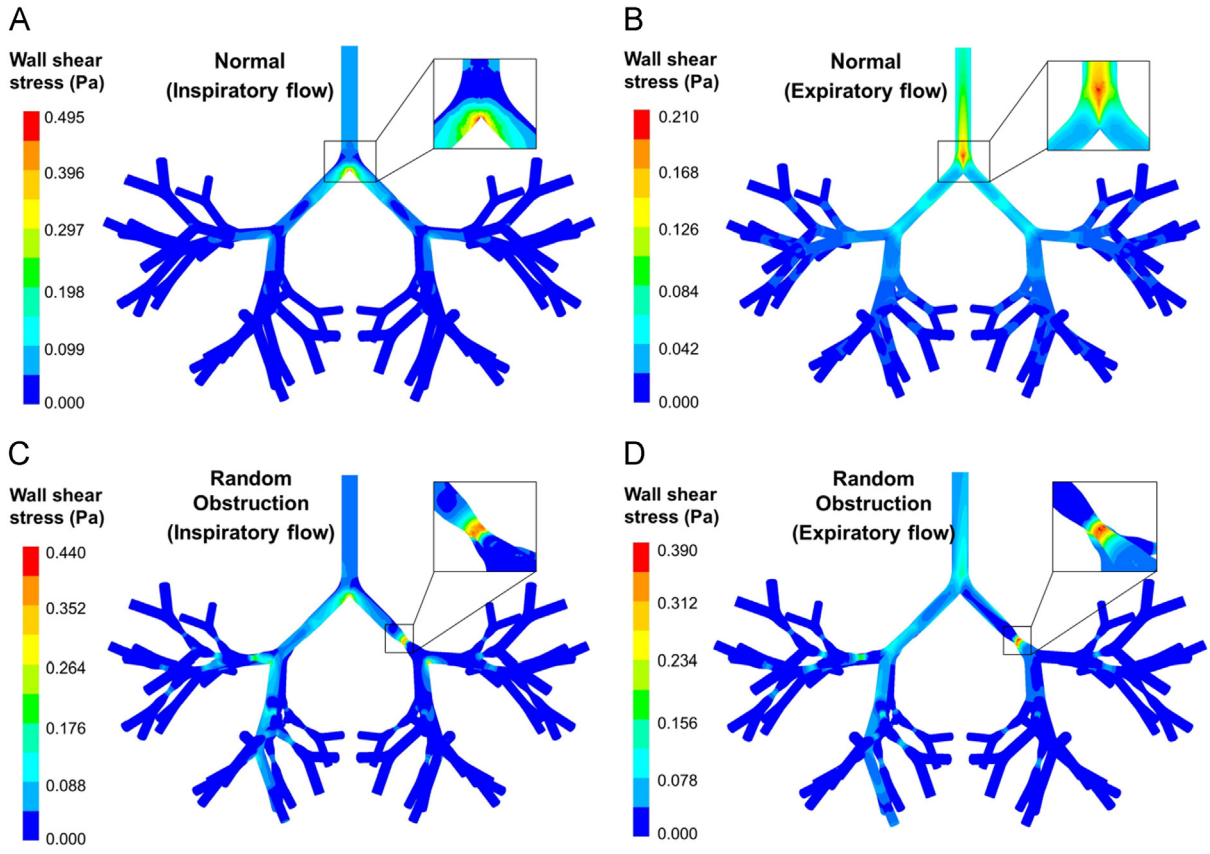

Fig. 7. Wall shear stress distribution in airway walls of the normal (A) and (B) and the random (C) and (D) obstruction models for high inspiratory and expiratory flows ($\Delta P = 18$ Pa). The locations of maximum shear stress are shown in the insets. (For interpretation of the references to color in this figure legend, the reader is referred to the web version of this article.)

3.4. *Airway constriction and wall shear stress*

Wall shear stress is the tangential force per unit area exerted on the airway wall due to airflow. Fig. 7 shows the wall shear stress distribution in the normal and obstructed peripheral airways for inspiratory and expiratory flows with the pressure drop of 18 Pa. For the normal airway model, wall shear stress was higher in the vicinity of the bifurcation compared to the tubular zone in each branch (Fig. 7(A)). For inspiratory flow, the maximum wall shear stress was observed at the edge of the inner wall of the first branch (i.e., the 8th generation) where the flow separates into two daughter branches. Because wall shear stress is proportional to the velocity gradient perpendicular to the flow direction, the location of the maximum shear stress was consistent with the skewed high-velocity region observed near the inner wall for inspiratory flow (Fig. 3(A)). Moreover, the velocity gradient in the flow was largest at the uppermost branch corresponding to the highest flow rate. For expiratory flow (Fig. 7(B)), higher values of wall shear stress compared with other regions in the airway were observed along the center of the upper branch where the airflows from the daughter branches merge and result in a high-velocity region (Fig. 4(A)). The maximum value of wall shear stress for the normal airway model during exhalation was near the bifurcation between the first branch (i.e., the 8th generation) and the second branches (i.e., the 9th generations) of the peripheral airways corresponding to the highest flow rate region in the airway.

In the obstructed airway models, contrary to the normal airway, the wall shear stress was higher at the airway walls constituting the constrictions for each branch compared with the bifurcations for both inhalation and exhalation (Figs. 7(C) and (D)). At the locally constricted passages, jet-like flows developed with increased stream velocity in the obstructed airways (Figs. 3 and 4). This, in turn, induced higher velocity gradients along the radial direction compared to other locations, increasing the wall shear stress. In all obstructed airway models, the maximum value of shear stress was observed on the constricted airway wall at the uppermost branch, i.e., at the 9th generation for the symmetric and asymmetric obstruction models (results not shown) and at the 10th generations for the random obstruction model (Fig. 7(D)).

Table 3 shows the maximum wall shear stress in each airway model for different rates of inspiratory and expiratory flows. We found that the wall shear stress was dependent on the flow rate for the same airway condition: the maximum wall shear stress increased, on average, by ~14-fold for a ~6-fold increase in flow rate (see Table 1). For inspiratory flow, the maximum shear stress values for the symmetric obstruction model were higher than those of the normal airway model due to the increase in flow velocity near the constriction, as discussed above. Similarly, in the asymmetric and random obstruction models, the maximum shear stresses were also induced near the constrictions in the obstructed branches. However, due to the presence of unobstructed branches in these models, the airflow rates through the obstructed branches were lower compared with those in the symmetric obstruction model. Therefore, the maximum shear stress values for the asymmetric and random obstruction models were lower compared with the symmetric obstruction model (Table 3).

For expiratory flow, the maximum wall shear stress values were higher for all the obstructed models compared with the normal airway model. Comparing across the obstructed models, the maximum wall shear stress value was the highest for the symmetric obstruction model, although the corresponding flow rate was the lowest. This was again due to the disproportionate distribution of airflow through the obstructed and unobstructed

Table 3
Maximum wall shear stress in the normal and obstructed airways.

Maximum wall shear stress (Pa)				
	Normal	Symmetric Obstruction	Asymmetric Obstruction	Random Obstruction
Inspiratory flow, ΔP (Pa)				
18	0.49	0.55	0.23	0.44
10	0.24	0.32	0.11	0.22
2	0.03	0.04	0.02	0.04
Expiratory flow, ΔP (Pa)				
18	0.21	0.52	0.26	0.39
10	0.10	0.27	0.13	0.21
2	0.01	0.04	0.02	0.04

branches in the random and asymmetric obstruction models. Between the random and the asymmetric obstruction models whose flow rates were similar, the maximum wall shear stress value was higher for the random obstruction model.

4. Discussion

4.1. Airflow patterns and airway resistance for normal and obstructed airways

In this study, we developed normal and obstructed CFD models of the peripheral lung region spanning the 8th to the 14th airway branches. To understand the pathophysiology of lower airway disease conditions, we ascertained how the airflow patterns were perturbed as a function of airway obstructions under different inspiratory and expiratory flow rates. We found that the airflow velocity and pressure magnitudes were significantly different between the normal and obstructed airways, as expected, due to the increased resistance to flow in the obstructed airways (Figs. 3 and 4). More importantly, the airflow patterns (the shape of velocity contours) were found to be markedly different both qualitatively and quantitatively for flow rates corresponding to more rigorous breathing conditions compared with the resting condition. The most important finding from our work was that the flow profiles demonstrated clear differences between normal and various disease conditions during exhalation (Fig. 4). Moreover, obstructions in relatively lower-generation branches were manifested in airflow patterns in the corresponding upper airway branches. These results not only help the understanding of airflow characteristics in lower airway diseases but could also potentially aid in developing and improving diagnostic techniques [46,47] based on imaging of airflow in the lungs.

In our comparison of airway resistance and airflow patterns between normal and obstructed airways, we showed that after the application of appropriate filters to avoid the inclusion of low- and near-wall velocities, airflow patterns had higher sensitivity than airway resistance in differentiating airway conditions. Although resistance values for the symmetrically obstructed airways were up to 80% higher than those for the normal airways, for the asymmetric and random obstruction models, the airway resistances were only 20% higher (Table 1). For the asymmetric and random models, which reflect more realistic cases, the resistance values themselves were within the normal variation for different breathing conditions [45]. The resistance we computed here represents airway resistance for only a portion of the peripheral lung region, which contributes $\leq 20\%$ to the total airway resistance for the entire airways [48]. Hence, we do not expect that the types of obstruction cases modeled in our study would be detectable by measurements of total airway resistance. Conversely, airflow patterns between normal and obstructed airways were distinctively different even for similar resistance values. The asymmetric and random obstruction models showed more inhomogeneous airflow patterns, distributing jet-like flows, and recirculation zones in local regions in the lungs (Figs. 3–5) and were distinct from normal geometries as gauged by correlation coefficient values close to 0.5 for high expiratory flows (Table 2).

One limitation of this work is that although histological measurements representative of obstructive airway conditions were included in the model in terms of a reduced surface area [26,28], we could not include the architecture of the obstructions due to unavailability of clinical data. We, therefore, used idealized geometries to represent the obstructions (Fig. 2). However, because we used smooth transitions of the geometry from the unobstructed airway sites to the obstructions, the effect of the obstruction architecture on the flow profiles was minimized. The actual obstructions are expected to be irregular and would, therefore, demonstrate even more heterogeneous changes in flow patterns compared to the normal unobstructed airway. With advancement in imaging methods, it may be possible to measure the actual structure of the airway obstructions, which could then be incorporated in the model. Another limitation of the work was that we assumed that both the healthy and diseased lungs would experience the same pressure differentials for the same breathing effort, which may not be valid for severely diseased cases [49,50]. Although the pressure differential needed to achieve adequate alveolar ventilation should be higher for the COPD lungs than for healthy cases, the capacity of the respiratory muscles to generate pressure decreases due to various biomechanical factors in diseased subjects [51]. As a result, it is difficult to correlate the change in pressure differential with the severity of the disease. In the absence of such data, we attempted to characterize the change in airflow characteristics using the same pressure differential for both healthy and diseased lungs.

4.2. Wall shear stress generated by airflow in obstructed airways

The wall shear stresses generated by airflow in the respiratory airways induce biologically relevant signals, such as a release of adenosine triphosphate (ATP) and an increase in intracellular

calcium concentration [52,53], that control the airway defense mechanisms. Moreover, wall shear stresses at low levels may enhance epithelial barrier function [52]. In contrast, excessive wall shear stresses may result in the damage of epithelial cells during airway collapse and reopening [54,55]. Therefore, it is essential to quantify the wall shear stresses induced by airflow for various disease conditions to assess the effect of obstruction on the airway physiology. In the absence of experimental methods to estimate wall shear stresses during respiration, computational modeling provides a critical recourse. Although modeling efforts have been made to estimate the wall shear stress in the central airways [56,57], it has not been characterized for lower airways. In this study, we calculated shear stress induced in the airway walls in the 8th to the 14th generations as a function of breathing rate and distribution of airway obstruction.

We observed that, for normal airways, the wall shear stress was highest near the bifurcations for both inspiratory and expiratory flows, as consistently shown in previous studies [56,57]. However, for obstructed airways, the maximum wall shear stress was induced near the constrictions. Consequently, one would expect the increased mechanical forces to result in aggravated pathological conditions in the regions of constrictions compared to unobstructed airways, as proposed in the past [58]. However, our model demonstrated that for flow rates <2300 ml/s (i.e., flow rates corresponding to heavy activities), the wall shear stress in both normal and obstructed airways was less than 0.3 Pa, which is within the physiological limit needed to promote respiratory defense mechanisms by enhancing epithelial barrier function [52]. Xia et al. [56] showed that wall shear stress in compliant airways decreases by 50% compared with rigid airways. Therefore, even for flow rates >4000 ml/s (corresponding to forced respiration rates), the maximum wall shear stress of ~ 0.5 Pa calculated by our model would be reduced if we considered airway compliance, which was neglected in our model. This implies that even during heavy activities, airflow-induced wall shear stress would not elicit damage to the airways, but rather would improve defense mechanisms by promoting epithelial barrier function [52]. To develop a better understanding of airway injury induced by shear stress, it is important to incorporate the liquid–solid interaction in the airway wall surfaces as well as the airway compliance. It has been suggested that epithelial cell damage occurs due to increased surface tension during airway reopening [54,55]. To model such a system, it would be necessary to develop a multi-scale model to describe cellular responses in addition to the global airflow distribution. Our work provides a starting framework to develop such a multi-scale model.

We further compared the airflow-induced wall shear stresses for different distributions of airway obstructions. Although the airway diameter was reduced by the same amount (50%) at the constricted locations for all obstructed models, the maximum shear stresses were widely different. In the symmetric obstruction model, the wall shear stress was highest compared to other obstructed models even though the flow rate was the lowest. The wall shear stress in the random obstruction model was as much as 2-fold higher than the asymmetric model, although their flow rates and airway resistance values were similar. These results demonstrate that the distribution of obstruction sites is an important factor in determining the wall shear stress. The local anatomical constrictions and the interconnectivity between unobstructed and obstructed branches significantly affect the accurate estimation of wall shear stresses, making the use of 3-D models critical. Although earlier models could describe the respiratory system by simplifying the 3-D lung airways into a network of one-dimensional branches [58,59], the details of 3-D flow and shear stress distributions as presented here could not be captured. In this study, we examined 3-D characteristics of airflow patterns and shear stress on the airway walls by comparing normal and obstructed airway models from the 8th to the 14th generations. These results facilitate the understanding of how lower airway diseases affect inspiratory and expiratory flow phases and wall shear stresses for various distributions of airway obstructions.

5. Summary

In this study, we investigated airflow characteristics in the lower airways of healthy and diseased human lungs using computational models. First, we developed 3-D airway models for the central and peripheral airways with different numbers of airway branches and validated the computational approach of using reduced number of airway generations to model respiratory airflow by comparing our results with *in vitro* experimental data from the literature. Next, we developed 3-D computational models for normal and obstructed lower airways. We included symmetric, asymmetric, and random obstructions in the airways between the 8th and 14th generations and compared airflow patterns, airway resistance, and wall shear stress under a range of breathing conditions. To facilitate a quantitative comparison of airflow patterns between the normal and obstructed airways, we obtained the Pearson's correlation coefficients for cross-sectional velocity contours after applying different filters to eliminate the low-velocity field near the airway walls. We found that, at high expiratory flows, the obstructions in relatively lower-generation branches were manifested in airflow patterns in the corresponding upper airway branches. We also demonstrated that airflow patterns subjected to filtering exhibited higher sensitivity than airway resistance for differentiating obstructed airways from the normal. Further, we showed that wall shear stresses were not only dependent on breathing rates and degree of obstruction, but also on the 3-D distribution of obstructions in the lower airways. For the same degree of obstruction and breathing rates, we noticed as much as two-fold differences in shear stresses, which could not be observed in previous one dimensional analytical models. In contrast to previous studies that propose increased wall shear stress due to obstructions as a possible damage mechanism for lower airways, our models demonstrated that for flow rates corresponding to heavy activities (<2500 ml/s), the wall shear stress in both normal and obstructed airways was less than 0.3 Pa, which is within the physiological limit needed to promote respiratory defense mechanisms. In conclusion, these results facilitate an understanding of how lower airway diseases affect inspiratory and expiratory flow phases and wall shear stresses.

Grants

This research was sponsored by the U.S. Army Network Science Initiative and a grant from the U.S. Department of Defense Health Program managed by the Military Operational Medicine Research Program, U.S. Army Medical Research and Materiel Command, Ft. Detrick, MD.

Disclosures

The opinions and assertions contained herein are the private views of the authors and are not to be construed as official or as reflecting the views of the U.S. Army or of the U.S. Department of Defense. This paper has been approved for public release with unlimited distribution.

Conflict of interest statement

M.J. Morris is on the Boehringer–Ingelheim/Pfizer Speaker's Bureau for Spiriva. The other authors have declared that no competing interests exist.

Acknowledgments

High-performance computing resources were made available by the U.S. Department of Defense High Performance Computing Modernization Program. The authors thank Dr. Ronald Poropatich for insightful and enlightening discussions.

Appendix A. Supplementary material

Supplementary data associated with this article can be found in the online version at http://dx.doi.org/10.1016/j.compbiomed.2014.06.008.

References

[1] World Health Organization, World Health Statistics 2008, ⟨http://www.who.int/whosis/whostat/2008/en/⟩, 2008.
[2] J.B. West, Pulmonary Pathophysiology: The Essentials, Wolters Kluwer Health/Lippincott Williams & Wilkins, Philadelphia, 2008.
[3] J. Vestbo, S.S. Hurd, A.G. Agusti, P.W. Jones, C. Vogelmeier, A. Anzueto, P.J. Barnes, L.M. Fabbri, F.J. Martinez, M. Nishimura, R.A. Stockley, D.D. Sin, R. Rodriguez-Roisin, Global strategy for the diagnosis, management, and prevention of chronic obstructive pulmonary disease: GOLD executive summary, Am. J. Respir. Crit. Care Med. 187 (2013) 347–365.
[4] D.B. Coultas, D. Mapel, R. Gagnon, E. Lydick, The health impact of undiagnosed airflow obstruction in a national sample of United States adults, Am. J. Respir. Crit. Care Med. 164 (2001) 372–377.
[5] S.K. Leung, W.W. Yew, C.C. Leung, Discordance in spirometric interpretations using different reference equations, Chest 136 (2009) 324–325 (author reply 325).
[6] R. Pellegrino, G. Viegi, V. Brusasco, R.O. Crapo, F. Burgos, R. Casaburi, A. Coates, C.P. van der Grinten, P. Gustafsson, J. Hankinson, R. Jensen, D.C. Johnson, N. MacIntyre, R. McKay, M.R. Miller, D. Navajas, O.F. Pedersen, J. Wanger, Interpretative strategies for lung function tests, Eur. Respir. J. 26 (2005) 948–968.
[7] M.J. Morris, V.X. Grbach, L.E. Deal, S.Y. Boyd, J.A. Morgan, J.E. Johnson, Evaluation of exertional dyspnea in the active duty patient: the diagnostic approach and the utility of clinical testing, Mil. Med. 167 (2002) 281–288.
[8] M. Salerno, T.A. Altes, J.R. Brookeman, E.E. de Lange, J.P. Mugler 3rd, Dynamic spiral MRI of pulmonary gas flow using hyperpolarized (3)He: preliminary studies in healthy and diseased lungs, Magn. Reson. Med. 46 (2001) 667–677.
[9] L. de Rochefort, X. Maitre, R. Fodil, L. Vial, B. Louis, D. Isabey, C. Croce, L. Darrasse, G. Apiou, G. Caillibotte, J. Bittoun, E. Durand, Phase-contrast velocimetry with hyperpolarized 3He for *in vitro* and *in vivo* characterization of airflow, Magn. Reson. Med. 55 (2006) 1318–1325.
[10] H.Y. Luo, Y. Liu, X.L. Yang, Particle deposition in obstructed airways, J. Biomech. 40 (2007) 3096–3104.
[11] C. Kleinstreuer, H. Shi, Z. Zhang, Computational analyses of a pressurized metered dose inhaler and a new drug-aerosol targeting methodology, J. Aerosol. Med. 20 (2007) 294–309.
[12] S.J. Jeong, W.S. Kim, S.J. Sung, Numerical investigation on the flow characteristics and aerodynamic force of the upper airway of patient with obstructive sleep apnea using computational fluid dynamics, Med. Eng. Phys. 29 (2007) 637–651.
[13] C. Xu, S. Sin, J.M. McDonough, J.K. Udupa, A. Guez, R. Arens, D.M. Wootton, Computational fluid dynamics modeling of the upper airway of children with obstructive sleep apnea syndrome in steady flow, J. Biomech. 39 (2006) 2043–2054.
[14] X.L. Yang, Y. Liu, H.Y. Luo, Respiratory flow in obstructed airways, J. Biomech. 39 (2006) 2743–2751.
[15] N.T. Tgavalekos, M. Tawhai, R.S. Harris, G. Musch, M. Vidal-Melo, J.G. Venegas, K.R. Lutchen, Identifying airways responsible for heterogeneous ventilation and mechanical dysfunction in asthma: an image functional modeling approach, J. Appl. Physiol. 99 (2005) 2388–2397.
[16] J.W. De Backer, W.G. Vos, S.C. Vinchurkar, R. Claes, A. Drollmann, D. Wulfrank, P.M. Parizel, P. Germonpre, W. De Backer, Validation of computational fluid dynamics in CT-based airway models with SPECT/CT, Radiology 257 (2010) 854–862.
[17] T. Gemci, V. Ponyavin, Y. Chen, H. Chen, R. Collins, Computational model of airflow in upper 17 generations of human respiratory tract, J. Biomech. 41 (2008) 2047–2054.
[18] D. Isabey, H.K. Chang, A model study of flow dynamics in human central airways. Part II: secondary flow velocities, Respir. Physiol. 49 (1982) 97–113.
[19] K. Horsfield, G. Cumming, Morphology of the bronchial tree in man, J. Appl. Physiol. 24 (1968) 373–383.
[20] K. Horsfield, G. Dart, D.E. Olson, G.F. Filley, G. Cumming, Models of the human bronchial tree, J. Appl. Physiol. 31 (1971) 207–217.
[21] X.L. Yang, Y. Liu, R.M. So, J.M. Yang, The effect of inlet velocity profile on the bifurcation COPD airway flow, Comput. Biol. Med. 36 (2006) 181–194.
[22] C. Kleinstreuer, Z. Zhang, An adjustable triple-bifurcation unit model for air-particle flow simulations in human tracheobronchial airways, J. Biomech. Eng. 131 (2009) 021007.
[23] Y. Liu, R.M. So, C.H. Zhang, Modeling the bifurcating flow in an asymmetric human lung airway, J. Biomech. 36 (2003) 951–959.
[24] C. van Ertbruggen, C. Hirsch, M. Paiva, Anatomically based three-dimensional model of airways to simulate flow and particle transport using computational fluid dynamics, J. Appl. Physiol. 98 (2005) 970–980.
[25] T.B. Martonen, Y. Yang, Z.Q. Xue, Effects of carinal ridge shapes on lung airstreams, Aerosol. Sci. Technol. 21 (1994) 119–136.
[26] J.C. Hogg, P.T. Macklem, W.M. Thurlbeck, Site and nature of airway obstruction in chronic obstructive lung disease, N. Engl. J. Med. 278 (1968) 1355–1360.
[27] M. Kikawada, Y. Ichinose, D. Miyamoto, K. Minemura, M. Takasaki, K. Toyama, Peripheral airway findings in chronic obstructive pulmonary disease using an ultrathin bronchoscope, Eur. Respir. J. 15 (2000) 105–108.
[28] J.E. McDonough, R. Yuan, M. Suzuki, N. Seyednejad, W.M. Elliott, P.G. Sanchez, A.C. Wright, W.B. Gefter, L. Litzky, H.O. Coxson, P.D. Pare, D.D. Sin, R.A. Pierce, J.C. Woods, A.M. McWilliams, J.R. Mayo, S.C. Lam, J.D. Cooper, J.C. Hogg, Small-airway obstruction and emphysema in chronic obstructive pulmonary disease, N. Engl. J. Med. 365 (2011) 1567–1575.
[29] C.G. Lausted, A.T. Johnson, W.H. Scott, M.M. Johnson, K.M. Coyne, D.C. Coursey, Maximum static inspiratory and expiratory pressures with different lung volumes, Biomed. Eng. Online 5 (2006) 29.
[30] D. Paek, F.D. McCool, Breathing patterns during varied activities, J. Appl. Physiol. 73 (1992) 887–893.
[31] J.L. Hankinson, J.R. Odencrantz, K.B. Fedan, Spirometric reference values from a sample of the general U.S. population, Am. J. Respir. Crit. Care Med. 159 (1999) 179–187.
[32] E.R. Weibel, Morphometry of the human lung: the state of the art after two decades, Bull. Eur. Physiopathol. Respir. 15 (1979) 999–1013.
[33] N. Nowak, P.P. Kakade, A.V. Annapragada, Computational fluid dynamics simulation of airflow and aerosol deposition in human lungs, Ann. Biomed. Eng. 31 (2003) 374–390.
[34] S.M. Dowdy, S. Wearden, D.M. Chilko, Statistics for Research, Wiley-Interscience, Hoboken, N.J., 2004.
[35] Z. Zhang, C. Kleinstreuer, C.S. Kim, Airflow and nanoparticle deposition in a 16-generation tracheobronchial airway model, Ann. Biomed. Eng. 36 (2008) 2095–2110.
[36] J. Choi, M.H. Tawhai, E.A. Hoffman, C.L. Lin, On intra- and intersubject variabilities of airflow in the human lungs, Phys. Fluids 21 (2009) 10191.
[37] A.S. Davies, C. Moores, The Respiratory System, Churchill Livingstone, New York, 2010.
[38] T.J. Pedley, R.C. Schroter, M.F. Sudlow, The prediction of pressure drop and variation of resistance within the human bronchial airways, Respir. Physiol. 9 (1970) 387–405.
[39] P. Evegren, L. Fuchs, J. Revstedt, On the secondary flow through bifurcating pipes, Phys. Fluid 22 (2010) 103601.
[40] R.C. Schroter, M.F. Sudlow, Flow patterns in models of the human bronchial airways, Respir. Physiol. 7 (1969) 341–355.
[41] Y. Zhao, B.B. Lieber, Steady inspiratory flow in a model symmetric bifurcation, J. Biomech. Eng. 116 (1994) 488–496.
[42] Y. Zhao, B.B. Lieber, Steady expiratory flow in a model symmetric bifurcation, J. Biomech. Eng. 116 (1994) 318–323.
[43] G.M. Allen, B.P. Shortall, T. Gemci, T.E. Corcoran, N.A. Chigier, Computational simulations of airflow in an in vitro model of the pediatric upper airways, J. Biomech. Eng. 126 (2004) 604–613.
[44] H. Schlichting, Boundary-layer Theory, McGraw-Hill, New York, 1968.
[45] P.W. Lord, J.M. Edwards, Variation in airways resistance when defined over different ranges of airflows, Thorax 33 (1978) 401–405.
[46] Y.S. Tzeng, K. Lutchen, M. Albert, The difference in ventilation heterogeneity between asthmatic and healthy subjects quantified using hyperpolarized 3He MRI, J. Appl. Physiol. 106 (2009) 813–822.
[47] M. Salerno, T.A. Altes, J.P. Mugler 3rd, M. Nakatsu, H. Hatabu, E.E. de Lange, Hyperpolarized noble gas MR imaging of the lung: potential clinical applications, Eur. J. Radiol. 40 (2001) 33–44.
[48] B.G. Ferris Jr., J. Mead, L.H. Opie, Partitioning of respiratory flow resistance in man, J. Appl. Physiol. 19 (1964) 653–658.
[49] D.F. Rochester, N.M. Braun, Determinants of maximal inspiratory pressure in chronic obstructive pulmonary disease, Am. Rev. Respir. Dis. 132 (1985) 42–47.
[50] F. Laghi, A. Jubran, A. Topeli, P.J. Fahey, E.R. Garrity Jr., J.M. Arcidi, D.J. de Pinto, L.C. Edwards, M.J. Tobin, Effect of lung volume reduction surgery on neuromechanical coupling of the diaphragm, Am. J. Respir. Crit. Care Med. 157 (1998) 475–483.
[51] S.Z. Newell, D.K. McKenzie, S.C. Gandevia, Inspiratory and skeletal muscle strength and endurance and diaphragmatic activation in patients with chronic airflow limitation, Thorax 44 (1989) 903–912.
[52] V.K. Sidhaye, K.S. Schweitzer, M.J. Caterina, L. Shimoda, L.S. King, Shear stress regulates aquaporin-5 and airway epithelial barrier function, Proc. Natl. Acad. Sci. USA 105 (2008) 3345–3350.
[53] R. Tarran, B. Button, M. Picher, A.M. Paradiso, C.M. Ribeiro, E.R. Lazarowski, L. Zhang, P.L. Collins, R.J. Pickles, J.J. Fredberg, R.C. Boucher, Normal and cystic fibrosis airway surface liquid homeostasis. The effects of phasic shear stress and viral infections, J. Biol. Chem. 280 (2005) 35751–35759.
[54] A.M. Bilek, K.C. Dee, D.P. Gaver 3rd, Mechanisms of surface-tension-induced epithelial cell damage in a model of pulmonary airway reopening, J. Appl. Physiol. 94 (770–783) (1985) 2003.
[55] D. Huh, H. Fujioka, Y.C. Tung, N. Futai, R. Paine 3rd, J.B. Grotberg, S. Takayama, Acoustically detectable cellular-level lung injury induced by fluid mechanical

stresses in microfluidic airway systems, Proc. Natl. Acad. Sci. USA 104 (2007) 18886–18891.
[56] G. Xia, M.H. Tawhai, E.A. Hoffman, C.L. Lin, Airway wall stiffening increases peak wall shear stress: a fluid-structure interaction study in rigid and compliant airways, Ann. Biomed. Eng. 38 (2010) 1836–1853.
[57] J.R. Cebral, R.M. Summers, Tracheal and central bronchial aerodynamics using virtual bronchoscopy and computational fluid dynamics, IEEE Trans. Med. Imaging 23 (2004) 1021–1033.
[58] G. Nucci, B. Suki, K. Lutchen, Modeling airflow-related shear stress during heterogeneous constriction and mechanical ventilation, J. Appl. Physiol. 95 (2003) 348–356.
[59] H.L. Gillis, K.R. Lutchen, How heterogeneous bronchoconstriction affects ventilation distribution in human lungs: a morphometric model, Ann. Biomed. Eng. 27 (1999) 14–22.